The origin of spin in galaxies: clues from simulations of atomic cooling halos

Joaquin Prieto[1,5,7*], Raul Jimenez[2,1,3], Zoltán Haiman[4], Roberto E. González[6,8]

[1] *ICC, University of Barcelona, Marti i Franques 1, E08028, Barcelona, Spain.*
[2] *ICREA.*
[3] *Institute for Applied Computational Science, Harvard University, MA 02138, USA.*
[4] *Department of Astronomy, Columbia University, 550 West 120th Street, MC 5246, New York, NY 10027, USA.*
[5] *Institute of Astronomy and NAO, Bulgarian Academy of Sciences, 72, Tsarigradsko Chaussee Blvd. 1784, Sofia, Bulgaria.*
[6] *Instituto de Astrofísica, Pontificia Universidad Católica de Chile, Av. Vicuña Mackenna 4860, Santiago, Chile.*
[7] *Departamento de Astronomía, Universidad de Chile, Casilla 36-D, Santiago, Chile.*
[8] *Centro de Astro-Ingeniería, Pontificia Universidad Católica de Chile, Av. Vicuña Mackenna 4860, Santiago, Chile*

16 October 2014

ABSTRACT

In order to elucidate the origin of spin in both dark matter and baryons in galaxies, we have performed hydrodynamical simulations from cosmological initial conditions. We study atomic cooling haloes in the redshift range $100 > z > 9$ with masses of order $10^9 M_\odot$ at redshift $z = 10$. We assume that the gas has primordial composition and that H_2-cooling and prior star-formation in the haloes have been suppressed. We present a comprehensive analysis of the gas and dark matter properties of four halos with very low ($\lambda \approx 0.01$), low ($\lambda \approx 0.04$), high ($\lambda \approx 0.06$) and very high ($\lambda \approx 0.1$) spin parameter. Our main conclusion is that the spin orientation and magnitude is initially well described by tidal torque linear theory, but later on is determined by the merging and accretion history of each halo. We provide evidence that the topology of the merging region, i.e. the number of colliding filaments, gives an accurate prediction for the spin of dark matter and gas: halos at the center of knots will have low spin while those in the center of filaments will have high spin. The spin of a halo is given by $\lambda \approx 0.05 \times \left(\frac{7.6}{\text{number of filaments}}\right)^{5.1}$.

Key words: galaxies: formation — large-scale structure of the universe — stars: formation — turbulence.

1 INTRODUCTION

Hoyle's seminal paper (Hoyle 1949) showed how angular momentum in galaxies can be generated via the tidal field of other galaxies. Later, Doroshkevich (1970) developed the tidal-torque theory within the framework of hierarchical galaxy formation, which determines the amplitude and direction of the spin of a dark matter halo based on the surrounding dark matter field (see Schaefer (2008) for a recent review). Numerical N-body simulations produce results that are in good agreement with the theoretical predictions, although linear theory is not always sufficient to determine the final angular momentum of a collapsed object (e.g. Barnes & Efstathiou (1987); Porciani et al. (2002) and references therein). In addition, mergers are expected to significantly alter a halo final spin (Vitvitska et al. 2002; Hetznecker & Burkert 2006; Davis & Natarajan 2010).

The amplitude of the dark matter halo spin influences the radius where baryons settle into a disc (White & Rees 1978; Fall & Efstathiou 1980), thus modifying its density and therefore the star formation history of the galaxy. The influence of spin on star formation history has been studied in detail (Toomre 1964; Dalcanton et al. 1997; Jimenez et al. 1997; Mo et al 1998; Avila-Rese et al. 1998). One interesting feature of tidal-torque theory in hierarchical models (Heavens & Peacock 1988; Catelan & Porciani 2001; Catelan et al. 2001; Crittenden et al. 2001; Porciani et al. 2002; Hahn et al. 2007) is the prediction of correlated spin directions and that the spin direction for dark haloes is strongly influenced by the halo environment. Pen, Lee & Seljak (2000) reported a detection of galaxy spin correlations at 97% confidence. Slosar et al. (2009) have measured the correlation function of the spin chirality and report, for the first time, a signal at scales $\lesssim 0.5$ Mpc h^{-1} at the $2 - 3\sigma$ level. Jimenez et al. (2010) showed how star formation in galaxies and current

---

* email:joaquin.prieto.brito@gmail.com

spin are correlated, with a 5σ detection of spin alignment among galaxies which formed most of their stars at $z > 2$.

Motivated by the theoretical study of Pichon & Bernardeu (1999), recent interest on the origin of spin in galaxies has focused on the effect of baryons on it. In a series of recent simulations Pichon et al. (2011) and Codis et al. (2012) have argued that spins may be generated entirely in the baryonic component due to the growth of eddies in the turbulence field generated by large-scales ($\gtrsim$ few Mpc) infall. If this was the case, it would imply that the final spin of halos is determined by the (random) properties of gas motions and the capability of the gas to generate eddies and vorticity. Their study focuses on DM haloes with masses in the range $10^{11} M_\odot \lesssim M_{vir} \lesssim 10^{14} M_\odot$; they found that the low mass haloes tend to have a spin parallel to their associated filament whereas the high mass haloes tend to have a spin perpendicular to their filament. They explained such correlation based on the shell crossing vorticity generation process (Pichon & Bernardeu 1999). In such a picture the low mass haloes are small enough to belong to a vortical region inside a filament. If this is the case, the DM spin (and its galaxy) will be aligned with the vortex vector. On the other hand, when the halo is too big to belong to a single vortex region its spin will be canceled and the main source of spin will be the angular momentum accreted through filaments. Such process will tend to create a spin vector perpendicular to the filament.

The above studies focused on DM haloes with masses $M_{vir} \gtrsim 10^{11} M_\odot$; in order study the very initial stages ($M_{vir} \sim 10^6 M_\odot$ and larger) of spin acquisition after the turn around we will work with haloes in the mass range of $M_{vir} \approx (1-2) \times 10^9 M_\odot$ at redshift $z \approx 10$.

In this paper we want to understand if the spin of primordial galaxies is provided by the dark matter or by random motions of the gas within the cosmic web. To this purpose we focused on simulating the properties of atomic cooling galaxies, which should be unaffected by stellar and AGN feedback processes. The possibility that the *James Web Space Telescope* (*JWST*) can observe the first galaxies, located in haloes $\gtrsim 10$ times more massive than those hosting the first PopIII stars, is an exciting motivation to study the so-called atomic cooling haloes (i. e. DM haloes with a virial temperature $T_{vir} \gtrsim 10^4$K; hereafter ACHs – see e.g. Ferrara (2010); Bromm & Yoshida (2011) for recent reviews).

Prieto, Jimenez, & Haiman (2013) showed how environment affects the final fate of ACH. Depending on the environment of the ACH, it could develop a disk or a very compact object. Motivated by this result, we further investigate the role of environment on ACH by studying their spin build up. In particular, we want to understand if location along a filament in the cosmic web or inside a knot, leads to different spin values for ACHs. It is worth clarifying that ACHs maybe not the dominant galaxy population at high-z as they require a strong UV background nearby to suppress H_2 formation. While rare, they exists (Fialkov et al. 2013) and thus can be clean laboratories of primordial galaxies without any effects due to previous stellar formation or feedback mechanisms.

For this purpose we have performed cosmological numerical simulations that describe the formation of ACH in different environments and with different values of the spin

parameter (λ). Our main finding is that the final spin value of a halo can be determined by the clustering of the dark matter. In particular, the topology where the halo resides determines the efficiency at which the initial (tidal torque originated) spin is destroyed or enhanced; the rate and direction of dark matter accretion determines the final fate of angular momentum.

This paper is organized as follows: in section §2 we describe the details of the numerical simulations and the halo sample. In §3, we describe our analysis and present the physical quantities extracted from the simulations. We conclude in §4.

2 METHODOLOGY AND NUMERICAL SIMULATION DETAILS

The simulations presented in this work were performed with the cosmological N-body hydrodynamical code RAMSES (Teyssier 2002). This code has been designed to study structure formation with high spatial resolution using the Adaptive Mesh Refinement (AMR) technique, with a tree-based data structure. The code solves the Euler equations with a gravitational term in an expanding universe using the second-order Godunov method (Piecewise Linear Method). The cooling module of the code has been replaced by the non-equilibrium cooling model for H+He primordial gas from the chemo-thermal KROME package (Prieto, Infante, & Jimenez 2008; Grassi et al. 2014).

Cosmological initial conditions were generated with the mpgrafic code (Prunet et al. 2008) inside a L=10 Mpc comoving side box. Cosmological parameters where taken from Planck Collaboration (2013): $\Omega_m = 0.3175$, $\Omega_\Lambda = 0.6825$, $\Omega_b = 0.04899$, $h = 0.6711$, $\sigma_8 = 0.83$ and $n_s = 0.9624$.

Using the parameters mentioned above, we ran a number of DM-only simulations with $N_p = 256^3$ particles starting at $z_{ini} = 100$. We selected four DM haloes of similar mass $M_{DM} \approx 10^9 M_\odot$ and different spin parameter

$$\lambda \equiv \frac{J}{\sqrt{2} M_{vir} R_{vir} V_{cir}} \tag{1}$$

(as defined in Bullock et al. (2001a)) at redshift $z = 10$. Here J, M_{vir}, R_{vir} and V_{cir} are the DM angular momentum, the halo virial mass, the halo virial radius and the halo circular velocity, respectively. The halo spin had values in the range $\lambda \approx 0.1 - 0.01$.

After the selection process we re-simulated the haloes including DM and atomic-only H+He primordial gas physics without star formation. For these simulations we re-centered the box in the DM halo position at redshift $z = 10$. These simulations were run using 3 DM nested grids filling the whole box. Each of these grids had 128^3, 256^3 and 512^3 DM particles (covering the refinement levels from 7 to 9). Furthermore, we inserted another DM grid of 512^3 particles centered at the box center covering 1/8 of the total box volume (corresponding to refinement level 10). In this way we were able to reach a DM resolution equivalent to a 1024^3 particles grid inside the box central region, which corresponds to a particle mass $m_p \approx 3 \times 10^4 M_\odot$ resolution.

Following a geometrical refinement strategy, we allowed refinements inside a fixed spherical volume centered at the simulation box center. The volume was big enough to prop-
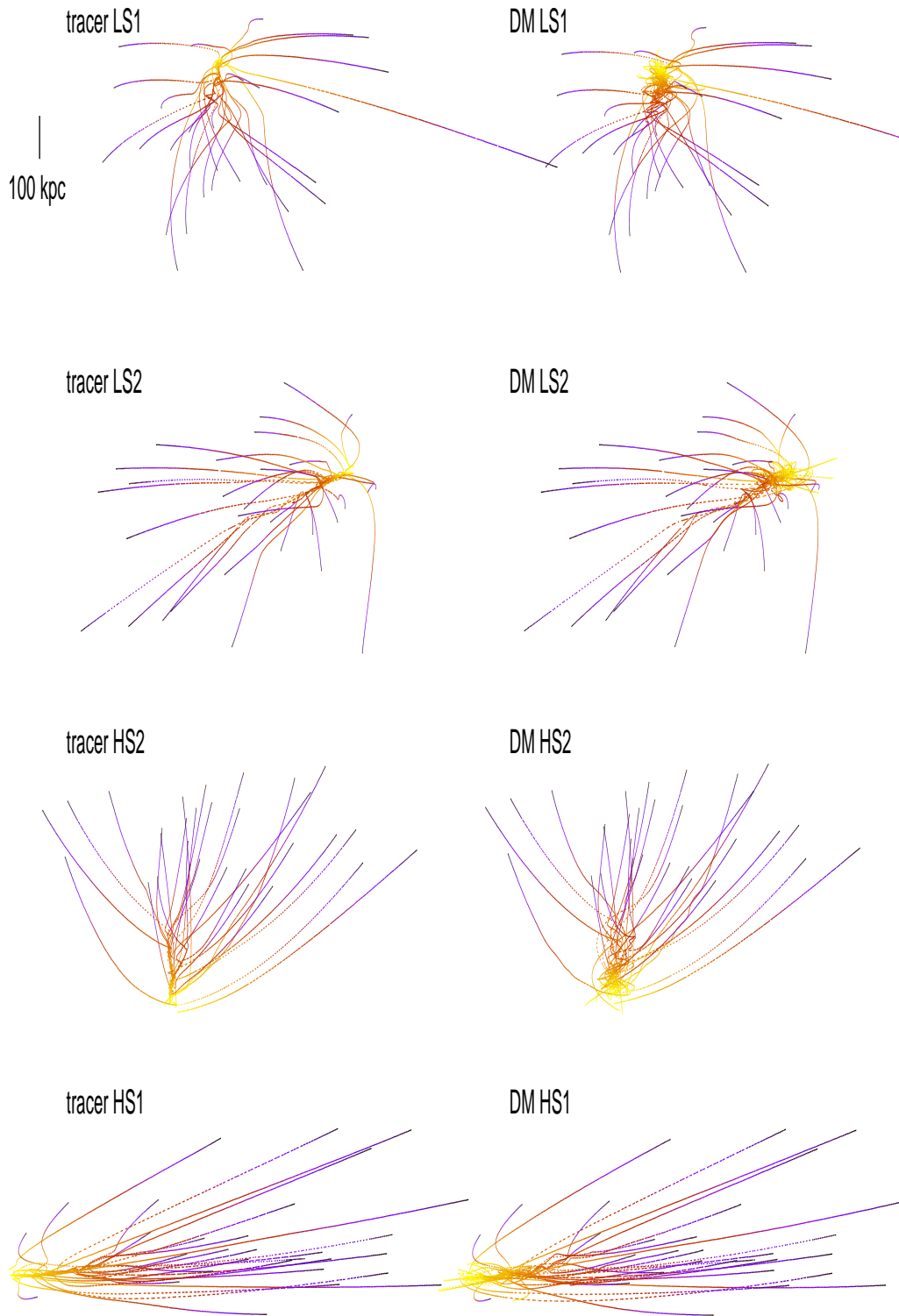
Figure 1. Trajectories of gas tracing particles (left) and DM particles (right) for the four different systems studied in this work. The trajectories are shown for particles within a radius of $0.5R_{\rm vir}$ at the end of the simulation. The time evolution is shown from $z \approx 100$ until $z \approx 9$ and it is color-coded with dark meaning early (high redshift) times and light meaning late (low redshift) times. Gas trajectories tend to be more concentrated than DM ones. Such behavior is the consequence of the gas cooling properties.
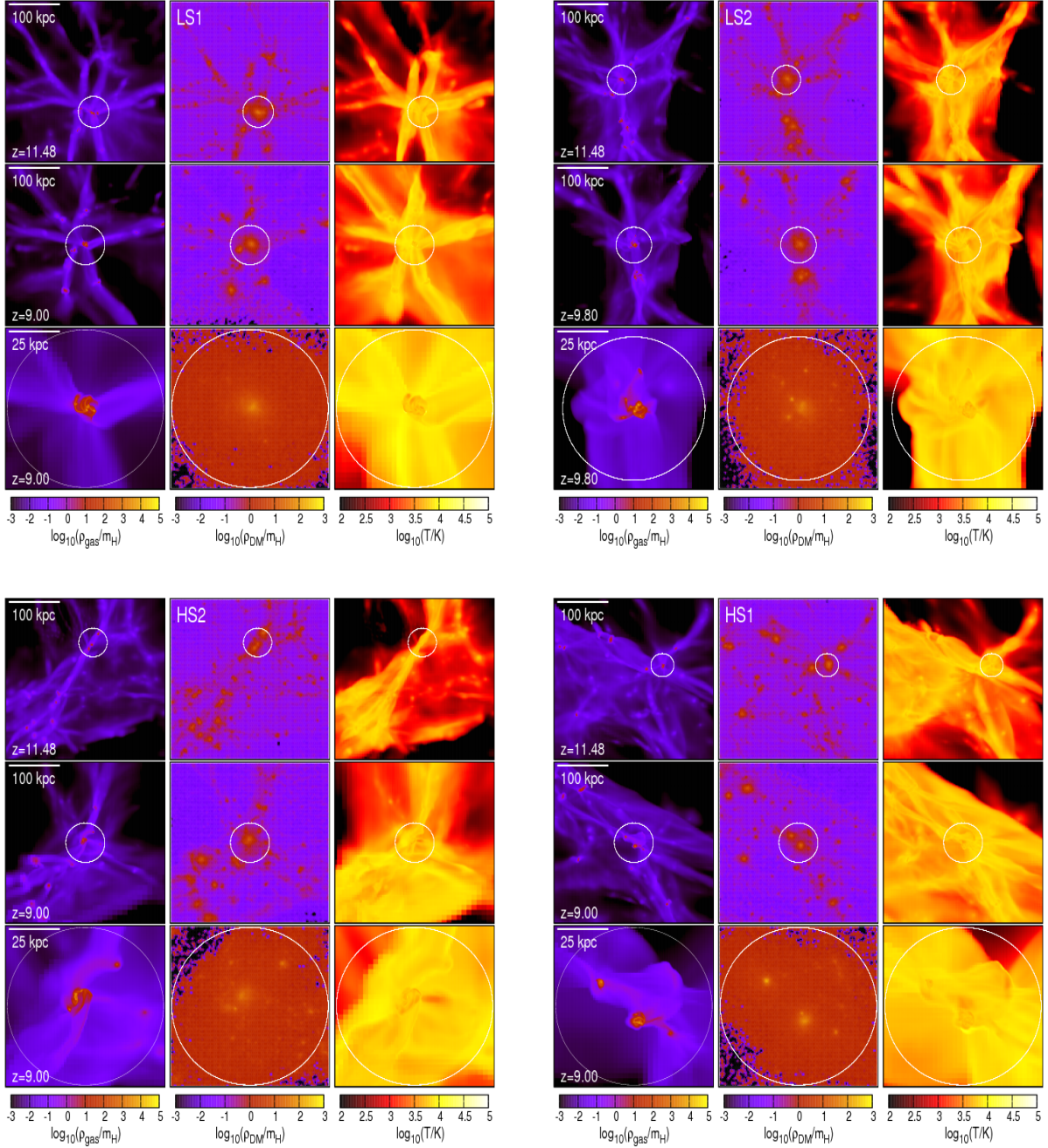
Figure 2. Mass weighted gas number density (left), DM number density (center) and gas temperature (right) for the four systems. The white circle shows the virial radius at a given redshift. Note the preference for LS systems to be located at center of knots in the cosmic web while LS systems are within filaments (see text for quantitative details).

erly resolve the whole Lagrangian patch finishing inside a radius $R_{ref} \approx 3R_{vir}$ at the end of the simulation, $z_{end} \approx 9$.

The refinement criterion was set as follows: a cell is refined if all of the following four conditions are fulfilled i) it contains more than 8 DM particles, ii) its baryonic content is 8 times higher than the average in the whole box, iii) the local Jeans length is resolved by less than 4 cells (Truelove et al. 1997), and iv) if the relative pressure variation between cells is larger than 2. Following these criteria the maximum level of refinement was set at $l_{max} = 16$, corresponding to

a co-moving maximum spatial resolution of $\Delta x_{max} \approx 153$ pc. To avoid numerical fragmentation due to the imposed maximum level of refinement we set an artificial temperature floor in order to reach the Jeans criterion when a cell at l_{max} satisfies one of the refinement conditions. However, due to the relatively high temperature of atomic cooling halos, this floor was never activated in the simulations presented in this paper. The floor generally activates for densities $> 10^4$ cm^{-3} and temperatures $< 300K$.

To compute the gas angular momentum we use tracer
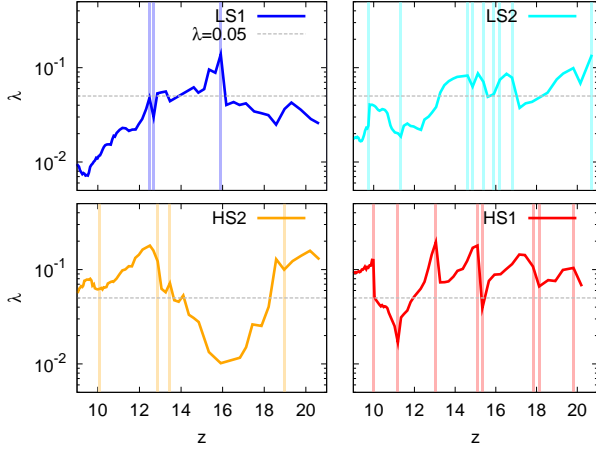
Figure 3. Lambda spin parameter as defined in Bullock et al. (2001a) for the four systems. We will use the same color convention for the next figures in the paper. The dashed gray line is $\lambda = 0.05$. Vertical lines show merger events as defined in the text. In general, merger events are associated to sharp variations of the spin parameter suggesting that these events can play a non negligible role in the DM halo spin acquisition process. The significant decrease and increase in spin for HS2 for $14 < z < 19$ is explained as the transition between isotropic matter accretion (decrease) and the formation of a filament that funnels matter into one preferred direction (increase). See more details in section 3.4 and Fig. 16.

(gas) particles to follow the Lagrangian patch associated to a given gas volume in our four re-simulations. Tracer particles were implemented in the same way as Dubois et al. (2012): for each DM particle there is a tracer particle (of zero mass) at the same position with zero initial velocity. It means that at the beginning the tracers have the same distribution of the DM particles. Based on the local gas velocity the tracer's position is updated following a simple forward Eulerian scheme. It means that at each time step the tracer moves following the local gas behavior. Fig. 1 shows the trajectories for both DM and tracer particles associated to the patch finishing inside $0.5R_{vir}$ at the end of the four simulations analyzed in this work (and presented in the next paragraph). From this figure it is possible to see how the gas trajectories are more concentrated than the DM trajectories. This feature is the consequence of gas cooling.

Based on the spin parameter of the analyzed haloes at redshift $z = 10$ we named our four simulations as HS1 ($\lambda \approx 0.1$), HS2 ($\lambda \approx 0.06$) and LS1 ($\lambda \approx 0.01$) and LS2 ($\lambda \approx 0.04$) where HS refers to High Spin and LS to Low Spin. In order to have an idea of the morphology of our haloes, Fig. 2 shows the mass weighted (gas and DM) density and gas temperature map for each system. The λ spin parameter evolution as a function of redshift is shown in Fig. 3.

3 RESULTS AND DISCUSSION

3.1 Initial Spin and Evolution of the Patch.

We study first the origin and evolution of spin before the virialization stage in order to compare it with the prediction from tidal torque theory. Initial angular momentum is acquired via tidal torques acting on the density field, the so-called tidal-torque theory (hereafter TTT: Peebles (1969); Doroshkevich (1970); White (1984)). TTT states that the initial angular momentum of an over-dense region in our Universe comes from tidal torques associated to the non-homogeneous gravitational field around it. Quantitatively:

$$L_i \propto a^2(t)\dot{D}(t)\epsilon_{ijk}T_{kl}I_{lj}, \qquad (2)$$

where L_i is the angular momentum of the region, $a(t)$ is the Universe's expansion scale factor, $D(t)$ is the linear perturbation theory growth factor, ϵ_{ijk} is the Levi-Civita symbol, T_{kl} is the tidal field tensor and I_{lj} is the moment of inertia tensor.

For a matter dominated universe, which is a good approximation for our Universe at redshift $z \gtrsim 10$, the time dependence of the above equation is

$$a^2(t)\dot{D}(t) \propto a^{3/2}(t). \qquad (3)$$

Fig. 4 shows the modulus of the specific angular momentum $\vec{J}$ (hereafter SAM) as a function of the expansion scale factor a_{exp} (top panel) and the misalignment angle θ (bottom panel) between the gas and DM components defined as

$$\cos(\theta) = \frac{\vec{J}_{DM} \cdot \vec{J}_{trc}}{|\vec{J}_{DM}||\vec{J}_{trc}|}, \qquad (4)$$

for each of the four simulated haloes. The figure shows the evolution of the patch associated to DM (solid line) and gas tracer particles (dashed line) inside R_{vir} at redshift $z = 10$. The SAM for both components was computed as

$$\vec{J}_{patch} = \sum_{parts.i} (\vec{r}_i - \vec{r}_{DM,CM}) \times (\vec{v}_i - \vec{v}_{DM,CM}). \qquad (5)$$

In the last expression the sum is applied to each type of particle (DM and tracers) inside the patch, $\vec{r}_i$ is the particle position at a given time, $\vec{r}_{DM,CM}$ is the DM center of mass position of the patch, $\vec{v}_i$ is the particle velocity and $\vec{v}_{DM,CM}$ is the DM center of mass velocity of the patch.

The vertical lines mark the merger events suffered by the main halo inside the patch. We only show merger events for which the mass ratio $M_2/M_1 \geq 0.1$, where M_2 is the mass of the secondary progenitor of the halo and M_1 is the mass of the main halo progenitor. Even if these merger events do not have a significant effect on the patch evolution they will be very relevant for the main halo evolution as will be shown in the next sub-section.

The grey dashed line in the figure shows $|\vec{J}_{patch}| \propto a^{3/2}(t)$. It is clear that both DM and gas tracer particles follow TTT predictions up to redshift $z \approx 20$. This value is in the vicinity of the turn-around redshift of the patch which is marked by a vertical grey line. After this redshift the patch's SAM starts to increase at a slower rate than before turn-around till it reaches an almost constant maximum value in the redshift range $z \approx 11 - 10$. After turn-around the gas SAM starts to fluctuate in short time scales. Such
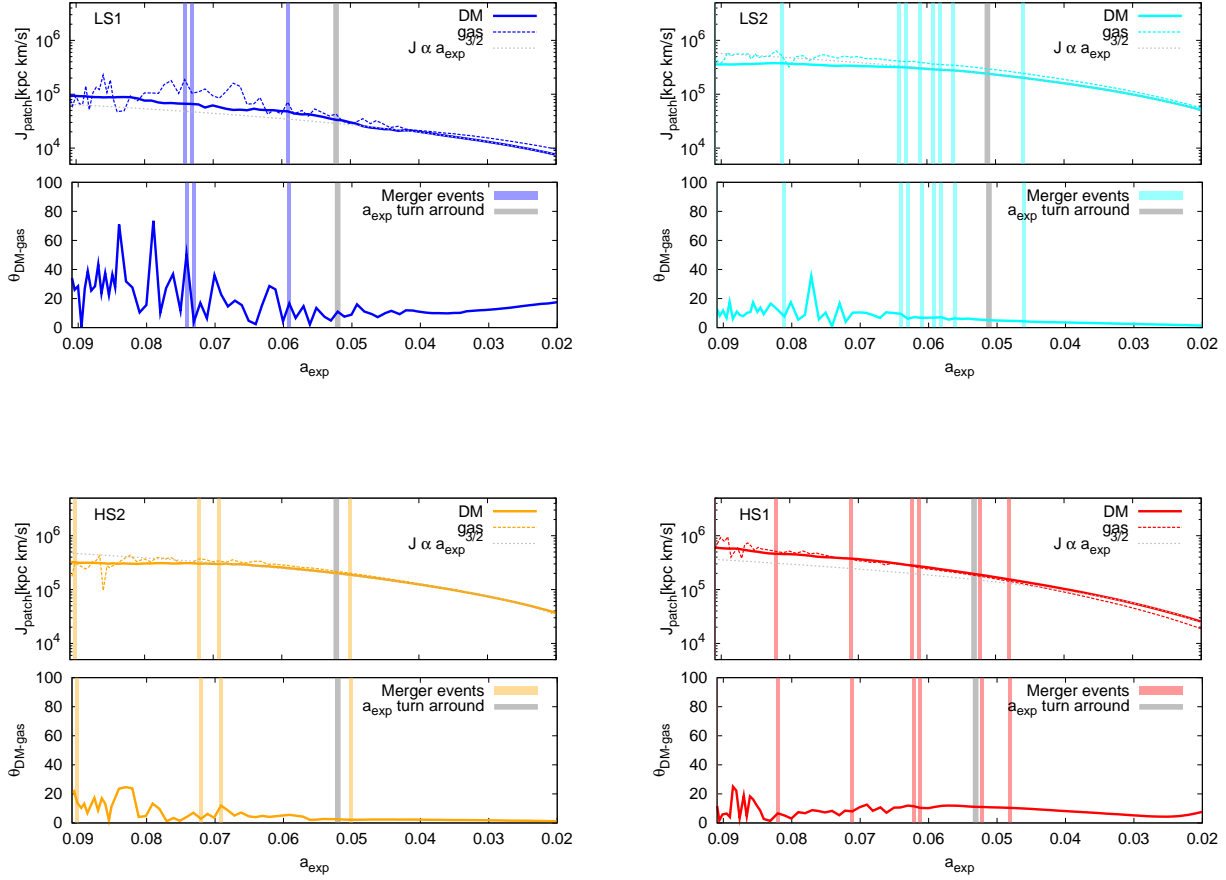
Figure 4. Specific angular momentum as a function of a_{exp} for a patch including all the particles inside the halo's virial radius at redshift $z = 10$ (top row of each panel). The solid line shows the DM particles evolution and the dashed line shows the gas tracer particles evolution. The dashed gray line shows the tidal torque theory prediction: $|J| \propto a_{exp}^{3/2}$. The blue vertical lines mark the merger events as defined in the text and the gray vertical line shows the DM patch turn-around. Misalignment angle between gas and DM angular momentum vectors as a function of a_{exp} (bottom row of each panel). The figure shows that at the beginning the DM patch follows a $|J| \propto a_{exp}^{3/2}$ evolution. At this stage the gas component follows roughly the same behavior with $\theta_{DM-gas} \lesssim 20°$. In the vicinity of the turn-around point the system deviates from the TTT prediction. Besides this deviation the gas component starts to show fluctuations in both the SAM and the misalignment angle. Some of these fluctuations are directly associated to merger events suggesting that these events are able to misalign the spin of both components via pressure gradients. Pressure torques associated to gas accretion are the source for these fluctuations between mergers.

fluctuations are not present in the DM SAM evolution. Because both components feel the same gravitational potential the most plausible explanation for this different behavior is the combination of cooling and collisional nature of the gas which after shell crossing is able to create torques associated to the gas gradient pressure, $\vec{r} \times \nabla P$.

The value of the misaligned angles showed in Fig. 4 are $\theta < 20°$ before turn-around. Such low values show that both gas and DM components tend to be aligned in the first stages of the patch evolution, i.e. both DM and gas feel the same gravitational potential around them and start to rotate in a similar way. In the vicinity of turn-around the misalignment angle starts to fluctuate showing variations at time scales much shorter than those associated to the DM SAM. The main source of such fluctuations is the non-linear

effects associated to the gas pressure gradient on the gas patch SAM as we will show in the next section.

3.2 Spin Evolution of the Main Halo.

After having analyzed the evolution of the SAM associated to the Lagrangian patch of the DM halo at $z = 10$, we study the behavior of the SAM associated to the material inside the virial radius of the main halo as a function of redshift. This quantity was computed using eq. 5 with the sum extended to all particles inside the virial radius of the halo at a given redshift.

Fig. 5 shows the same quantities as in Fig. 4 but for the main halo as a function of redshift. From the four panels of this figure we can see that the SAM modulus of both
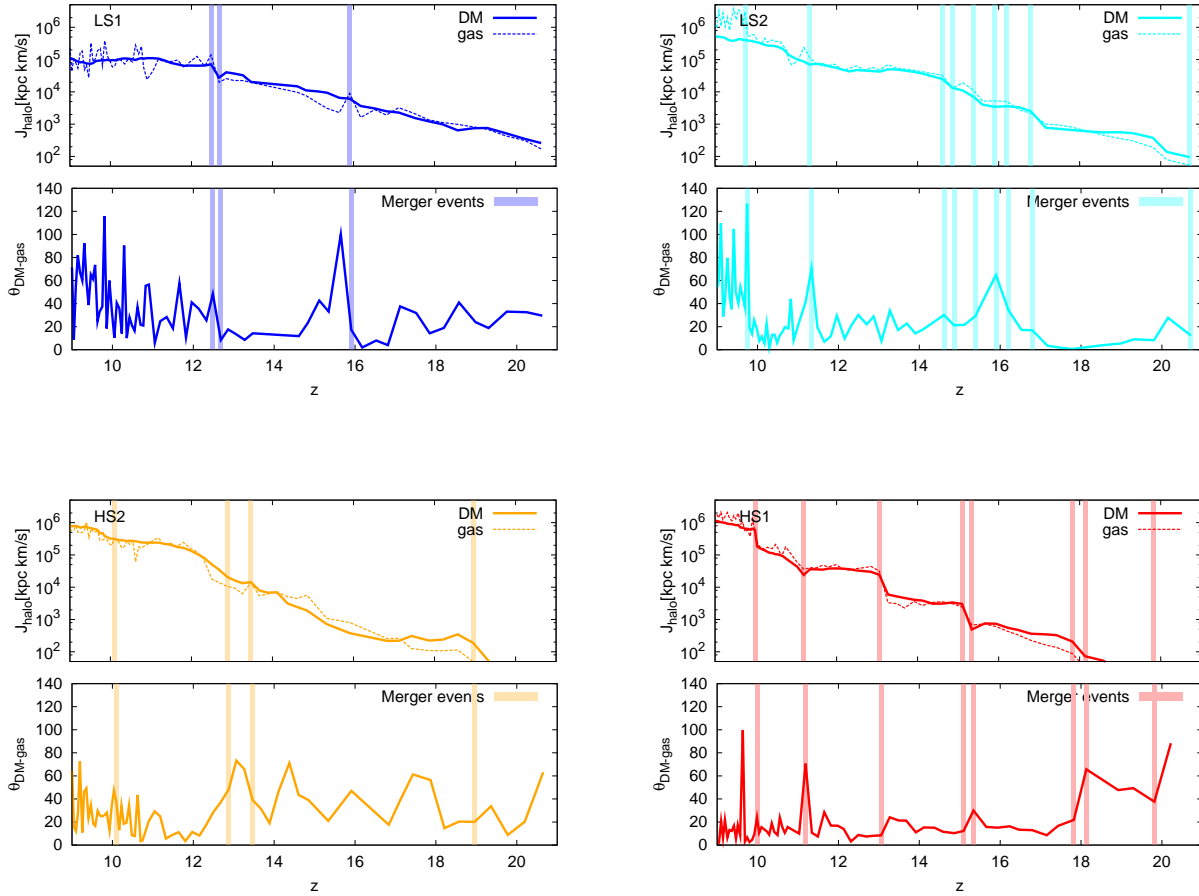
Figure 5. Specific angular momentum for the halo as a function of redshift z (top row of each of the four panels). Solid line: DM component of the system. Dashed line: the gas component of the system. The vertical lines mark merger events as defined in the text. Misalignment angle θ between the spin of both the DM and the gas component of the halo (bottom row of each panel). The figure shows that the merger events are able to produce strong variations in the misalignment angle. The halo spins up between mergers suggesting that accreted material plays an important role in the angular momentum acquisition process (see Fig. 7). Fluctuations of the misalignment angle where there are no mergers suggest that the accretion process is able to misalign the spin of both components due to pressure torques.

DM and gas follow the same trend but the gas component exhibits greater fluctuations than the DM evolution.

We computed the misalignment angle between the gas and DM SAM inside the virial radius using eq. 4. In contrast with the result of Fig. 4, for the single halo SAM it is possible to see a correlation between some merger events (marked by vertical lines in Fig. 5) and the misalignment angle of the different components. Such correlations are present in the four systems and are the manifestation of pressure gradients working on the gas due to the violent interaction between the dense central regions of the halo progenitor. Besides the fluctuations associated to occasional merger events, there are fluctuations between the vertical lines also. Such fluctuations are associated to pressure torques triggered by soft accretion (including mergers with a mass ratio $M_2/M_1 < 0.1$) into the halo central region.

Fluctuations in the gas SAM are originated by gas pressure torques which depend on the temperature and density, which are strongly modified by the cooling. Since there is

a temperature floor ($T \sim 10^4$K) for the gas, the gas gets denser and the pressure increases, in other words, isothermal collapse will always put the gas onto a higher adiabat, compared to a fixed adiabat with no cooling. It is therefore natural that cooling will change the dominant torque, increasing it given that pressure gradients will increase. This torque (which does not affect the DM evolution) can decouple the gas evolution from the DM evolution creating the short time scale variations in the gas SAM. To quantify the role of pressure torques at causing fluctuations and spin angle misalignment in the gas component, we compute the acceleration associated to the pressure gradient for a typical merger event and compared it to the gravitational acceleration associated to the gravitational potential gradient, in particular we computed

$$a_{gas} = \frac{|\nabla P|}{\rho} \quad \text{versus} \quad a_{grav} = |-\nabla\Phi|. \qquad (6)$$

Fig. 6 shows this before, during and after a merger for the
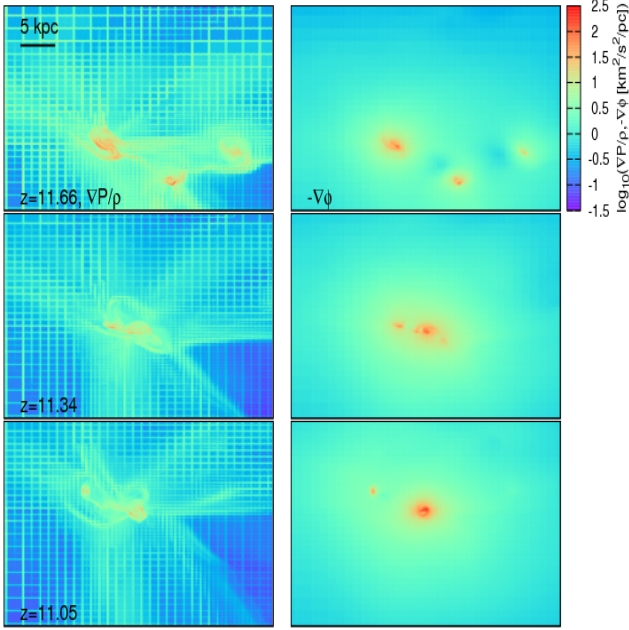
Figure 6. Acceleration associated to pressure gradient (left) and gravity gradient (right) maps for a merger event for halo LS1 before, during and after the merger. Pressure gradient which only the gas feels are comparable in magnitude to gravity gradients, which both DM and gas feel. These pressure gradient (and its associated torque), due both to cooling of the gas and density enhancements due to turbulent motion, provide an extra source of spin generation for the gas.

LS1 halo. Pressure gradients (and its associated torque) are comparable to gravitational ones in the high density regions. Within our analysis it is not possible to determine if the pressure torques are dominated by cooling of the gas or by the collisional nature of the gas that after shell crossing provides pressure induced torques. We will investigate this in an upcoming publication.

It is interesting to have a direct comparison between the two analysis presented above, i.e. a patch v/s main halo evolution. Fig. 7 shows the SAM evolution for the four systems (for gas and DM). The thick lines correspond to the patch evolution and the thin lines to the main halo evolution. Our two extreme spin cases, namely LS1 (top-left) and HS1 (bottom-right), have very different behaviors. Whereas the LS1 halo shows three merger events barely disturbing the SAM value and a soft mass accretion producing an almost constant slope in the main halo SAM evolution, the HS1 halo presents merger events which drastically change the SAM value. These changes in the SAM value (and in the λ evolution, see figure Fig. 3) are captured as steps in the figure, a feature that does not appear in the LS1 halo. Such step-like structure shows that in this case mergers contribute significantly to the SAM of the final halo. The other two intermediate cases (LS2 and HS2) show a mixed behavior with periods of constant SAM slope and step-like evolution due to mergers.
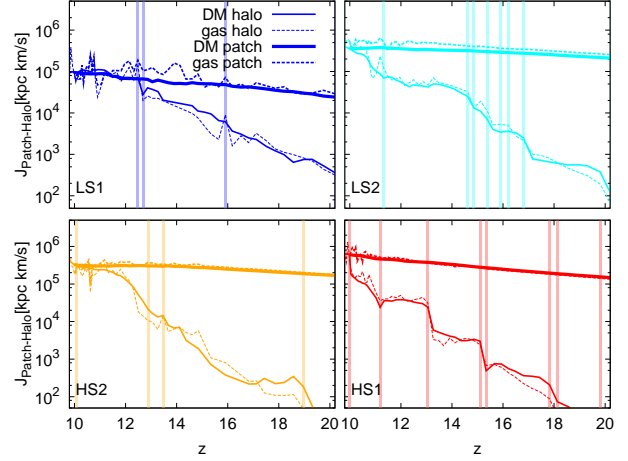
Figure 7. Evolution of both the main halo specific angular momentum (thin line) and the specific angular momentum of the patch associated to the main halo at redshift $z = 10$ (thick line) for each of the four systems. Solid line: DM component and in dashed line is the gas component of the systems. From this it is possible to see that the halo's final ($z = 10$) specific angular momentum comes from two sources: i) mergers, indicated by vertical lines and ii) accretion between merger events. The lowest λ halo (LS1) shows a main halo spin evolution with a roughly constant slope barely disturbed by 3 merger events. This behavior suggests that in this system most of the angular momentum comes from soft accreted material. On the other hand, the highest λ halo (HS1) shows a staircase-like (far from constant slope) evolution where each of the steps is associated to merger events. The other two cases, LS2 and HS2, show a mixed behavior with periods of constant slope evolution and jumps associated to a stair like (mergers) evolution.

3.3 Accretion and Mergers.

After showing how the main halo builds up its SAM from merger events and mass accretion it is worth to study these processes in more detail. In order to do so we computed the mass accretion history of the haloes, the SAM flux into each halo and the SAM acquisition from accreted material and the merged secondary halo for a single merger event. Together, all these quantities allow us to infer how the haloes at high redshift acquire their spin.

We start with the accretion features in our four systems. Fig. 8 shows the gas and DM mass accretion history for each of our four haloes. The mass accretion at a given redshift was computed as the ratio

$$\frac{d\mathrm{M}(z(\mathrm{t}))}{d\mathrm{t}} = \frac{\mathrm{M_{vir}(t + \Delta t) - M_{vir}(t)}}{\Delta \mathrm{t}} \qquad (7)$$

From this figure it is not easy to find dramatic differences between the four systems. The most clear difference is associated to the merger history of the haloes. The haloes with more mergers tend to have more peaks in the gas accretion evolution. This feature is directly associated to the large amount of mass accreted in a short time step. Another difference shows up when we compare the DM mass accretion of the LS1 halo with the other three systems. In the
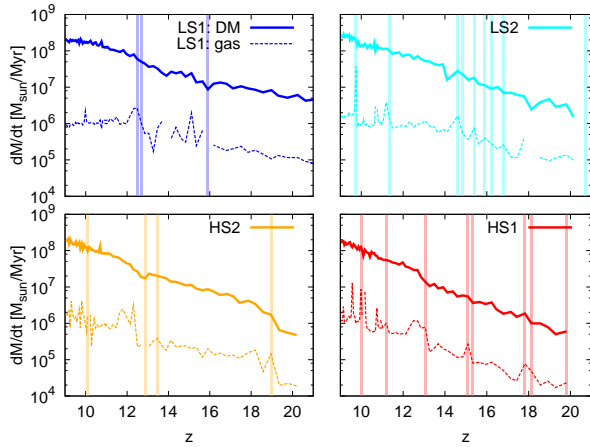
Figure 8. Mass accretion evolution. DM evolution (solid line) and gas evolution (dashed line).
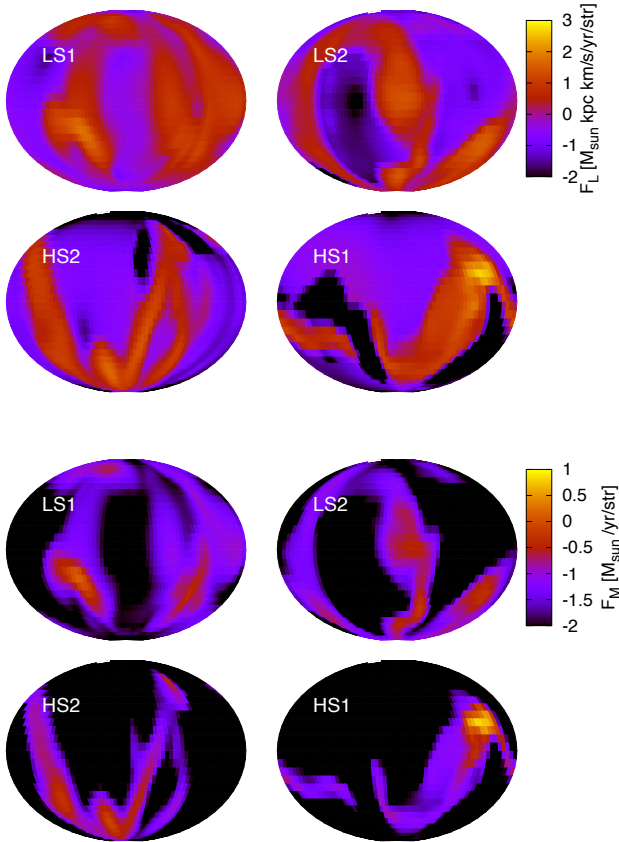
Figure 9. Mollweide projections. Top: mass weighted angular momentum flux for each of the four systems. For the low spin systems the angular momentum flux is more isotropic than for the high-spin system, which is more concentrated along a preferred axis. The difference between LS1 and HS1 is especially striking. Bottom: mass weighted mass accretion for each of the four systems. High angular momentum flux regions match to the high mass flux regions. Such a relation suggests that most of the system's angular momentum inside the sphere of 0.5R$_{\rm vir}$ is coming from the accreted mass.

lowest spin halo (LS1) the DM accretion evolution shows a slower slope compared with the others[1].

Fig. 9 shows Mollweide projections of the distribution of mass weighted in-falling gas angular momentum flux (in units of M$_\odot$ kpc km/s/yr/str) at $z = 10$ for the four different haloes at the top panel and the mass accretion flux (in units of M$_\odot$ /yr/str) at the bottom panel. The angular momentum flux was computed as

$$F_{\rm L} = \sum_{\rm shell(\Delta r)} \rho r^2 |\vec{r} \times (\vec{v} - \vec{v}_{\rm CM.gas})| \hat{r} \cdot (\vec{v} - \vec{v}_{\rm CM.gas}), \qquad (8)$$

where the sum was performed including all cells at position $\vec{r}$ inside a spherical shell of radius $|\vec{r}| \equiv r = 0.5 R_{\rm vir}$ and thickness $\Delta r = 4\Delta x$, with Δx the cell side at the maximum level of refinement; $\hat{r}$ is the unitary vector in the $\vec{r}$ direction. In the same way the mass flux was computed as

$$F_{\rm mass} = \sum_{\rm shell(\Delta r)} \rho r^2 \hat{r} \cdot (\vec{v} - \vec{v}_{\rm CM.gas}). \qquad (9)$$

From the figure (bottom panel) it is possible to see that the two fast rotating haloes HS2 and HS1 tend to acquire angular momentum flux from a preferred hemisphere, from south and north, respectively. Another interesting remark is that both LS1 and LS2 are acquiring angular momentum from nearly all directions without a preferred angle. From the bottom panel it is possible to see that the high angular momentum flux regions are good matched to the high mass flux regions. Such a correlation suggests that most of the angular momentum accreted on the halo's central region is coming with the accreted mass (as has been seen in more massive systems by Powell et al. (2011) and Dubois et al. (2012)).

Keeping the above analysis in mind, it is useful to look at Fig. 10 (and Fig. 2). This figure shows the tracer particles vector velocity field inside a sphere of radius R ∼ 300 co-moving kpc around the corresponding halo colored by the initial SAM value at redshift $z \approx 70$. The two red arrows located at the main halo center depict the DM SAM (solid line) and the gas SAM (dashed line) inside the virial radius. The vector field is shown at two different redshifts in order to illustrate the time evolution of the systems. The two most slowly rotating haloes, LS1 and LS2, show a mostly radial accretion channeled through a number of filaments with the vector spin placed at the convergence point of the filaments. On the other hand, the two fastest rotating systems, HS1 and HS2, develop a filament like structure with the halo vector spin more or less perpendicular to it. These suggest a relation between the structures around DM haloes, their gas in-falling pattern and their spin: haloes surrounded by a number of filaments tend to cancel out their accreted/merged SAM whereas haloes located in the middle of a filament tend to receive the accreted/merged SAM from a preferred direction resulting in a higher spin halo.

We now turn our attention to the number of mergers that take place in each of the main haloes. Because the number of mergers happening in the main four haloes is ≈ 25,

---

[1] Due to the definition based on the virial mass, there are some points with no data in the figure. This is because in some steps the halo defined by the halo finder keeps its mass constant or it is slightly reduced.
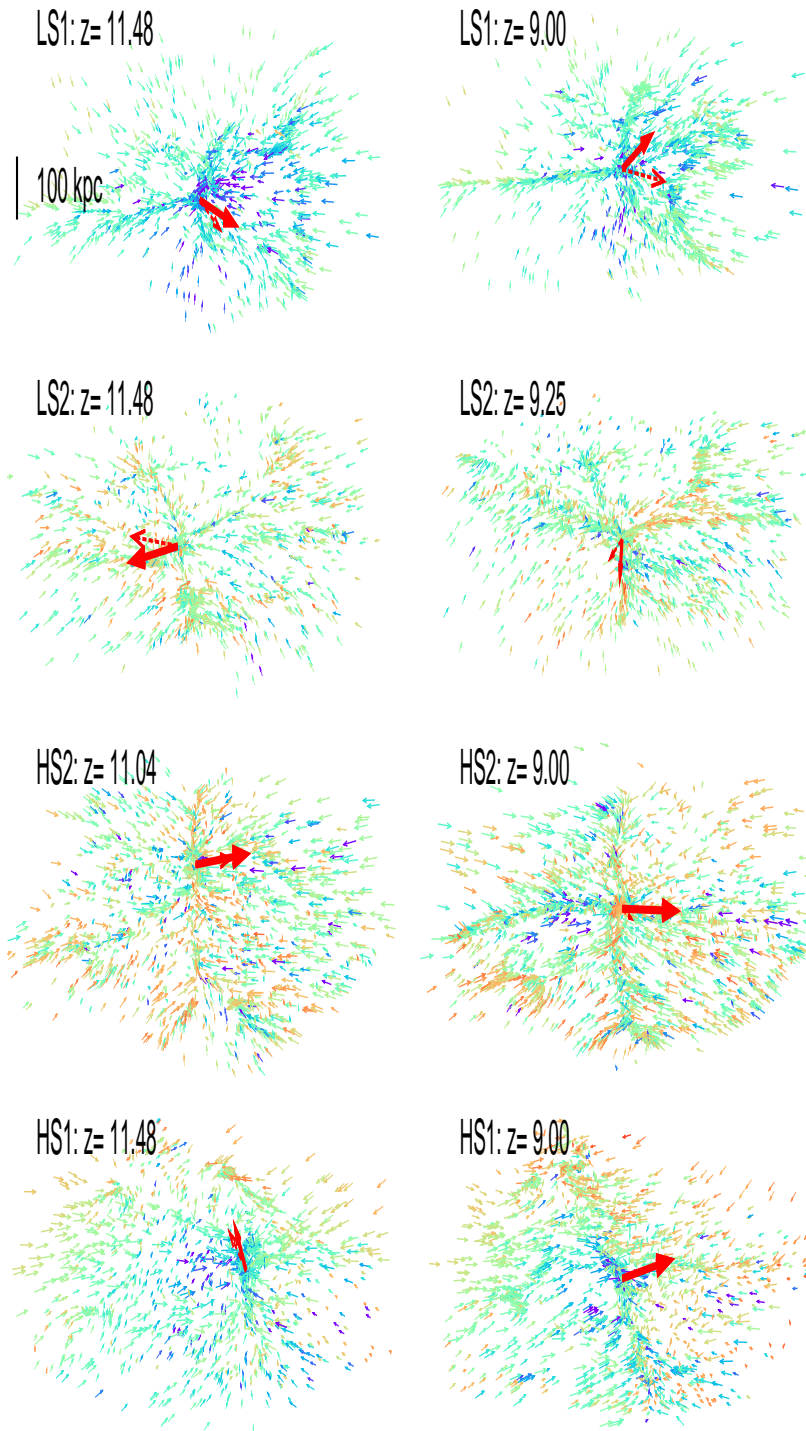
Figure 10. Tracer particle's velocity vector field for the low spin (top) and the high spin systems (bottom) at two different moments. The different colors show the specific angular momentum of each particle at $z \approx 70$. Red indicates high values and magenta low values. The red arrows show the specific angular momentum of the main central halo for gas (in dashed line) and DM (in solid line).
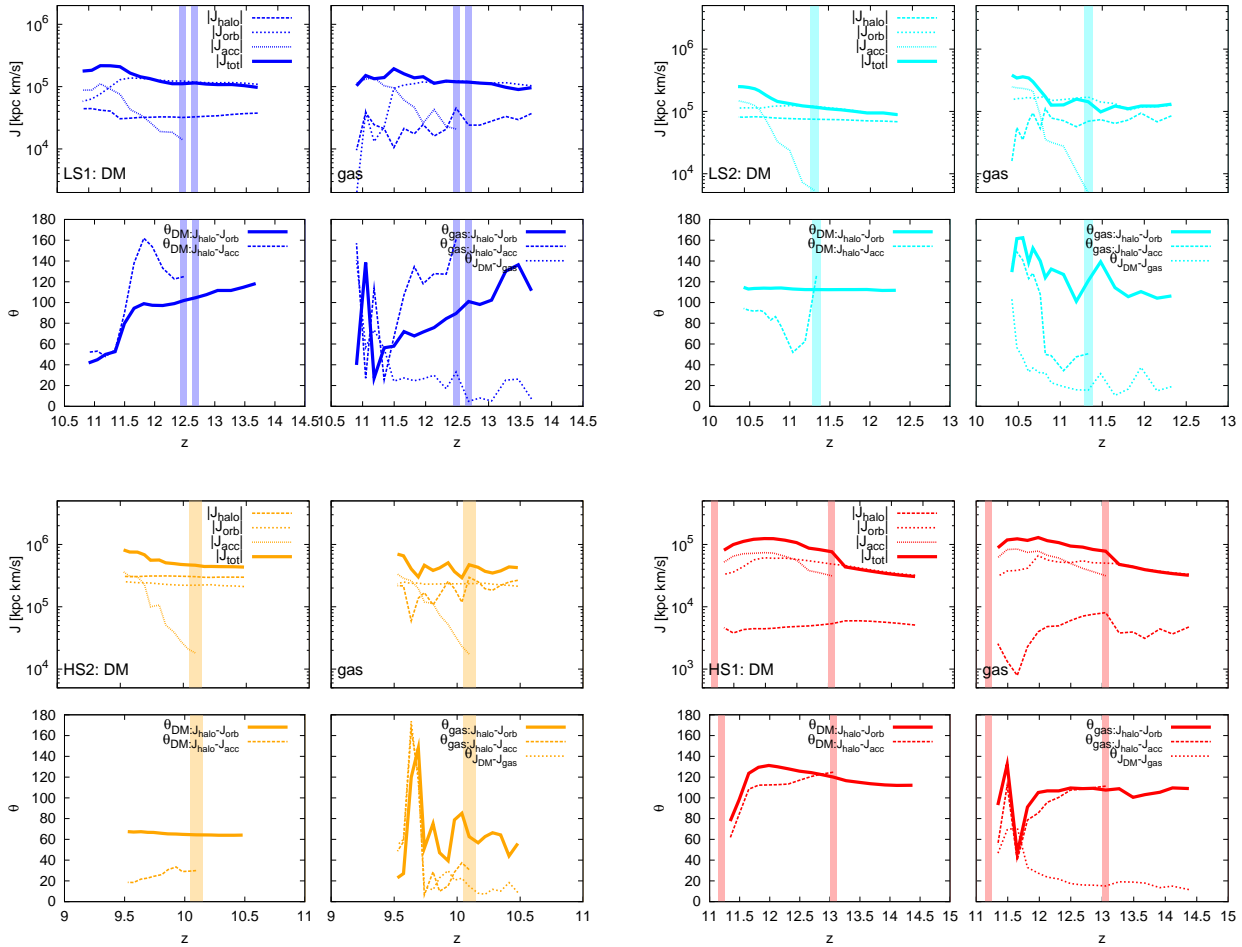
Figure 11. Top panels: Specific angular momentum evolution in a merger event (DM at left, gas at right). The angular momentum is computed from the main progenitor's DM particles center of mass during its evolution with redshift. The long-dashed line shows the main halo specific angular momentum; short-dashed line: the orbital angular momentum of the secondary progenitor of the final halo; dotted line: the specific angular momentum of the accreted material (which appears after the merger marked by the vertical line); solid line: the vectorial addition of these three components. Bottom panels: Angle between the three different angular momentum vectors. The solid line is the angle between the main halo's spin and the secondary progenitor's spin; long-dashed line: the angle between the main halo's spin and the spin of the accreted material. The short-dashed line in the bottom right panel shows the gas-DM misalignment angle of the particles associated to the main halo progenitor before the merger. The figure shows that the main halo spin is much lower than the orbital angular momentum of the secondary progenitor before the merger (this is not a general trend, see the HS2 case at bottom left). After the merger, the accreted material starts to increases its relative importance with respect to the orbital angular momentum. This continues until the accreted material dominates the source of angular momentum with respect to the main halo DM center of mass. The bottom panels show that different angular momentum components are not necessarily aligned due to the complex geometry of the process. This explains why the vectorial addition is not the dominant line in the top panels. The large fluctuations of the gas angles in the last stage of the evolutionary patch coincide with the merger of the high density central regions of the two main progenitors.

they are too many as to describe each of them in detail. Therefore we will focus on a particular merger event per system[2].

Fig. 11 shows the SAM and misalignment angle through a given merger event for each one of our haloes. As in previous figures the vertical lines shown the redshift of the merger event. The SAM evolution shown on the top rows is de-

composed as follows: the long dashed line corresponds to the main halo SAM with respect to its own center of mass $|\vec{J}_{\mathrm{halo}}|$; the short dashed line shows the orbital SAM (with respect to the main halo center of mass) associated to the secondary halo going to merge with the main one, $|\vec{J}_{\mathrm{orb}}|$; the dotted line corresponds to the accreted SAM (with respect to the main halo center of mass), $|\vec{J}_{\mathrm{acc}}|$, note that this line will appear after the vertical line showing the merger event; finally the solid line is the modulus of the vectorial addition of the previous quantities: $|\vec{J}_{\mathrm{tot}}| = |\vec{J}_{\mathrm{halo}} + \vec{J}_{\mathrm{orb}} + \vec{J}_{\mathrm{acc}}|$.

In three of the four systems (LS1, LS2, HS1) $|\vec{J}_{\mathrm{orb}}|$ dominates the SAM before the merger. In the merger associated to the HS2 halo, $|\vec{J}_{\mathrm{halo}}|$ is slightly larger than $|\vec{J}_{\mathrm{orb}}|$ before

---

[2] We will show that the merger events are a generic process that can be described taking into account three SAM sources: the main halo one, the secondary halo one and the soft accreted one. With these three SAM sources we can fully describe the process.
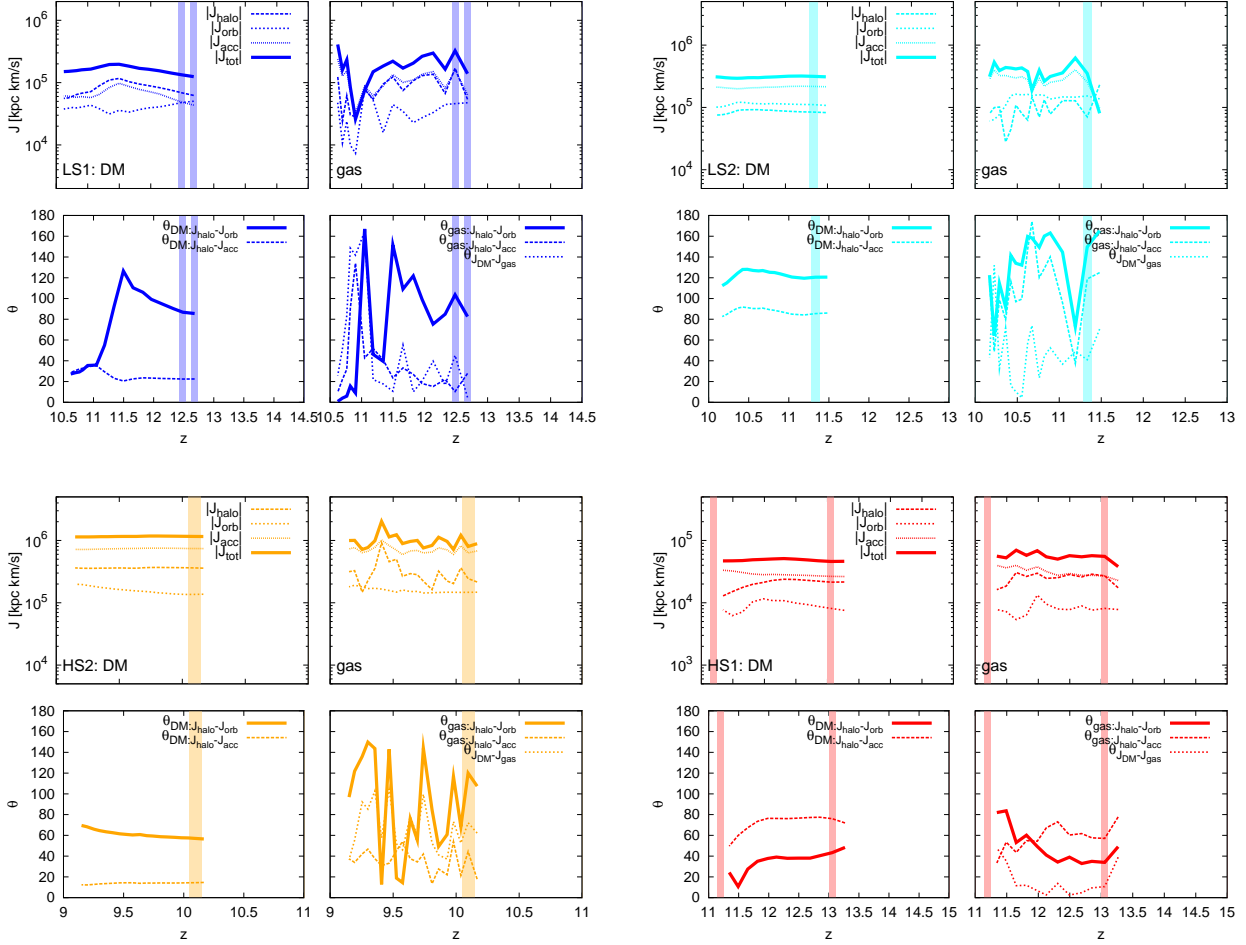
Figure 12. Same as Fig. 11 but for the patch associated to particles (gas and DM) inside the corresponding virial radius after the merger. The patch is selected at $\Delta z \approx 1.5$ after the merger event marked by the vertical lines.

the merger. This results tell us that from the main halo position the secondary halo going to merge brings a substantial amount of SAM to the new system (mainly due to the long radius $\vec{r}$ in the SAM $\vec{r} \times \vec{v}$ computation). Despite of this trend, it is interesting to note that after the merger the accreted material becomes the main source of SAM in the four mergers shown here.

The bottom row of our four panels shows the misalignment angle between different components of the $\vec{J}_{\text{tot}}$ vector. The different lines are: misalignment angle θ between $\vec{J}_{\text{halo}}$ and $\vec{J}_{\text{orb}}$ in solid line; θ between $\vec{J}_{\text{halo}}$ and $\vec{J}_{\text{acc}}$ in long dashed line and θ between $\vec{J}_{\text{gas}}$ and $\vec{J}_{\text{DM}}$ in short dashed line. All different SAM components are not aligned. The misalignment between all the different components is a consequence of partial cancellation of the total SAM. This phenomenon can be seen in the fact that $|\vec{J}_{\text{tot}}| \leq |\vec{J}_{\text{halo}}| + |\vec{J}_{\text{orb}}| + |\vec{J}_{\text{acc}}|$ in all cases. The misalignment angle associated to the gas component fluctuates significantly after the merger events. It can be explained by the pressure waves created when the dense central regions of the progenitors interact. Such process is able to create pressure torques, as explained in the previous section, resulting in a misalignment between the

gas SAM components. Such torques are not present in the DM.

We have also computed the SAM associated to a patch after the merger. In order to do so we have identified the particles inside the virial radius of the main halo at $\Delta z \approx 1.5$ after the merger event. Furthermore, we identified the particles belonging to the main and to the secondary halo before the merger. With these definitions we marked as the accreted material all the particles belonging to the final halo and not belonging either to the main nor the secondary halo. This is shown in Fig. 12. The main difference with Fig. 11 is that from the patch center of mass the orbital angular momentum associated to the secondary halo is not the dominant spin source of the system (mainly due to the decrease of the radius $\vec{r}$ in the SAM $\vec{r} \times \vec{v}$ computation). In three (LS2, HS2 and HS1) of the four systems the main source of spin is associated to accreted material. The bigger the Δz the higher the contribution from accreted material, thus we can conclude that in a system suffering a few mergers the softly accreted material will dominate the SAM source. Only in one (LS1) system the dominant source of spin is coming from the main halo. In this case the difference between the accreted and the main halo contribution is a factor < 2: they are almost the

same. The total DM SAM of the patch is almost constant in the considered redshift range.

Table 1 and table 2 show all the relevant information about the merger processes with respect to the main halo (labeled with 1) center of mass for DM and gas, respectively. Two interesting remarks based on these tables are that the LS systems have an average mass merger ratio (M_2/M_1) lower than the HS systems and that the average angular momentum ratio (J_2/J_1) is higher for the HS systems compared to the LS ones.

3.4 Filaments and Environment.

The environmental conditions around DM haloes seem to play a relevant role in the spin acquisition process (as previously suggested by Pichon et al. (2011) but with a less detailed study as the one shown here). Because of this it is worth to study in more detail the filamentary structure of each halo and their position in the cosmic web.

Here it is useful to come back to Fig. 2. If we look at the first row of the systems LS1 (top left) and LS2 (top right) it is clear that around $z \approx 11.5$ the main halos of these two systems were surrounded by a number $(N_f \sim 8)$ of filaments converging into a knot. Such special location creates a necessary condition for the SAM cancellation inside the virial radius. In such location all the material (accreted and merged) bringing a given amount of SAM will be able to cancel the total SAM value if from another direction is coming material with a comparable amount of SAM but pointing in another direction (which seems to be the general case as shown in Fig. 11 and Fig. 9). This process can explain the low spin associated to these two haloes below $z \approx 11$.

Looking at the first row of Fig. 2 for the high spin systems, HS1 (bottom right) and HS2 (bottom left), we observe that at $z \approx 11.5$ they are not in a knot of the cosmic web (as in the LS cases). While the HS2 halo is the composition of three over-densities (the result of two mergers around $z \approx 13$, see Fig. 5) inside a thin filament of length $L_f \gtrsim 200$ co-moving kpc, the HS1 halo has a single over-density in the center and it is going to merge with a secondary halo belonging to a thin filament of length $L_f \approx 100$ co-moving kpc pointing to the top right corner of the box (this will be the merger associated to the vertical line at $z \approx 10$ in Fig. 5). These systems suffered important mergers at $z < 14$. Looking at table 1 the average merger mass ratio is higher for the HS systems compared with the LS systems and the same trend can be seen in the haloes spin ratio. Such features suggest that mergers are an important source of spin in the HS systems.

In order to quantify the results presented above we compute the filamentary structure of our systems. We compute at each snapshot the direction of the largest filaments connected to the main halo center. Filaments are computed using the DisPerSE code (Sousbie 2011), which computes for a particle distribution the Delaunay tessellation and uses discrete Morse theory to characterise the topology of the density field, i.e. critical/saddle points, lines and surfaces. Filaments are then traced by the saddle points connecting two local maximum critical points. The advantages of this method are: i) it is scale-free thus filaments are purely defined by the point distribution, and a persistence threshold defined as the "number of sigmas" with respect to Poisson
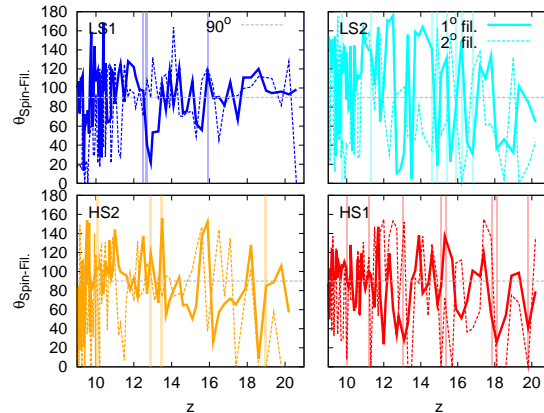
Figure 15. Angle between the DM halo spin and the two main filaments associated to the same halo as a function of redshift for our four systems. The solid line corresponds to the main filament and the dashed line to the second main filament. The dashed gray line in the four panels marks a 90° angle orientation.

noise. ii) there is no smoothing involved in the density field computation; it uses directly the Delaunay tessellation, then it uses all available data specially useful to resolve filaments in poorly sampled fields with few particles. iii) only the direction of the filaments is needed, thus only filament skeletons are required and not the thickness or filament membership computed by more sophisticated methods.

The filaments directions are computed for each snapshot in the following way:

• We run DisPerSE code with a persistence threshold of 4σ. This parameter is tuned to find only strong filaments which correlate very well with a visual inspection or other methods where typical filaments have a density contrast at least $\simeq 10$ times above average density (Colberg et al. 2005; Gonzalez & Padilla 2010).

• From the filaments found in this way, we select only those which reach the central halo. That is, the filaments containing a critical point matching the FOF halo center.

• Filaments are ranked by length and number of bifurcations/segments.

• We compute the filament direction by averaging the filament path from the halo center up to a distance of 50 kpc or $3 \times R_{vir}$ depending on which value is smaller. We found in general that filaments are quite straight and radial at close distances, but beyond a few virial radii they warp and bifurcate into smaller filaments, making it hard to define a global filament direction.

• The final most relevant filament is chosen by visual inspection among the few filaments detected automatically, and results are in very good agreement between human and automated criterion, this last step is mostly intended to check consistency.

Fig. 13 and 14 show the DM structure for our four systems with the filamentary structure (in red lines) computed following the prescription described above. These figures show the DM evolution (in different columns) from two different almost perpendicular angles (in different rows).

LS1
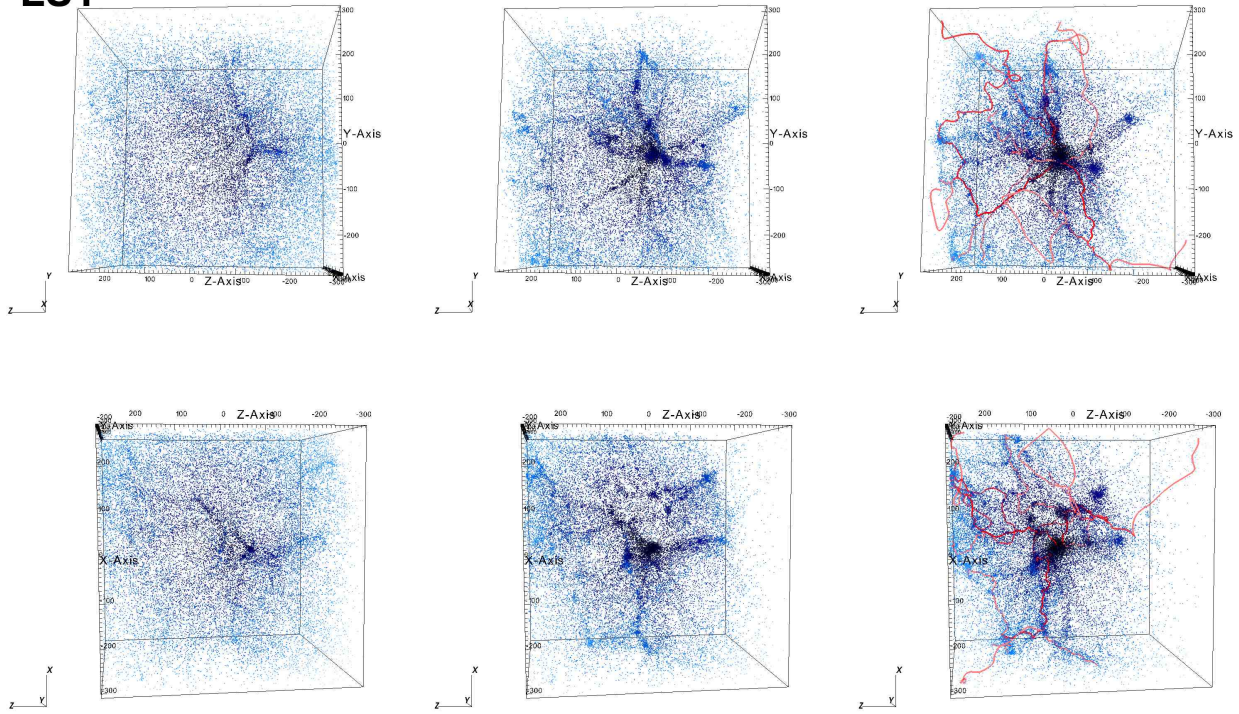
LS2
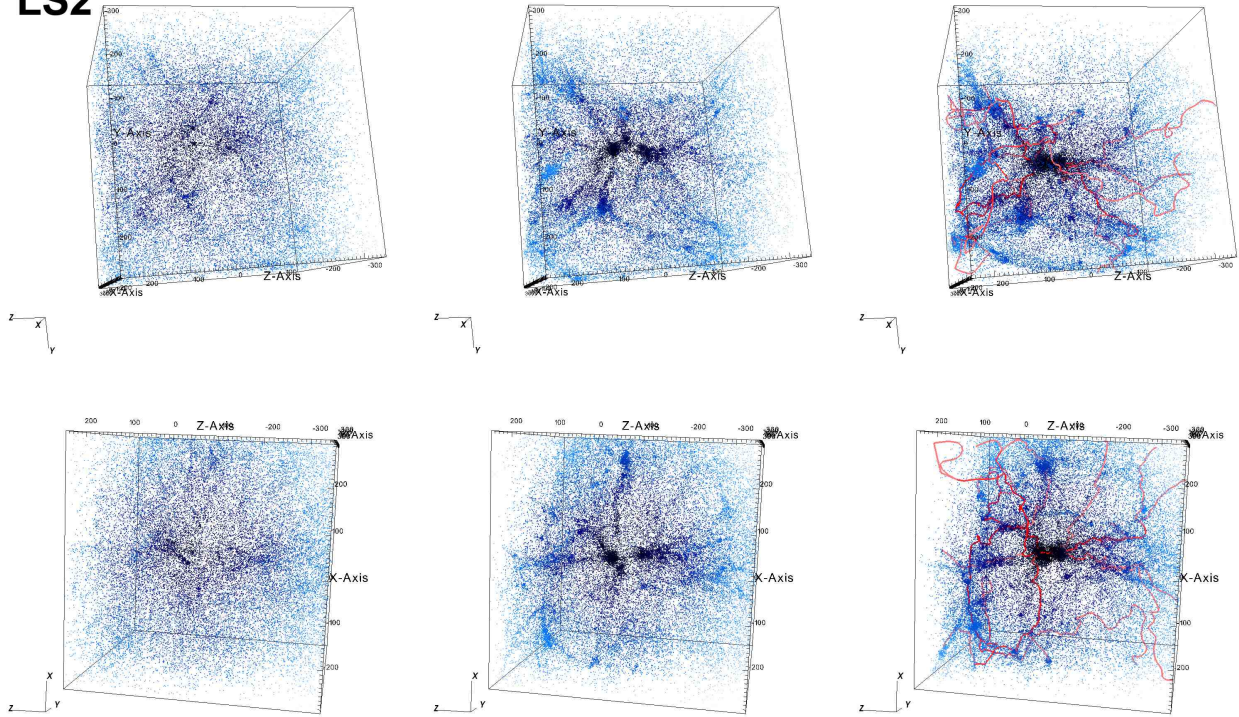
Figure 13. LS DM evolution (in different columns) from different views (in different rows). The first two rows correspond to the LS1 system and the last two rows correspond to the LS2 system. From the figure it is clear that both systems are located inside a knot surrounded by a number of filaments marked by red lines in the last column, corresponding to the final redshift of the simulations, $z = 9$. Such condition provides an efficient spin cancellation inside the virial radius.
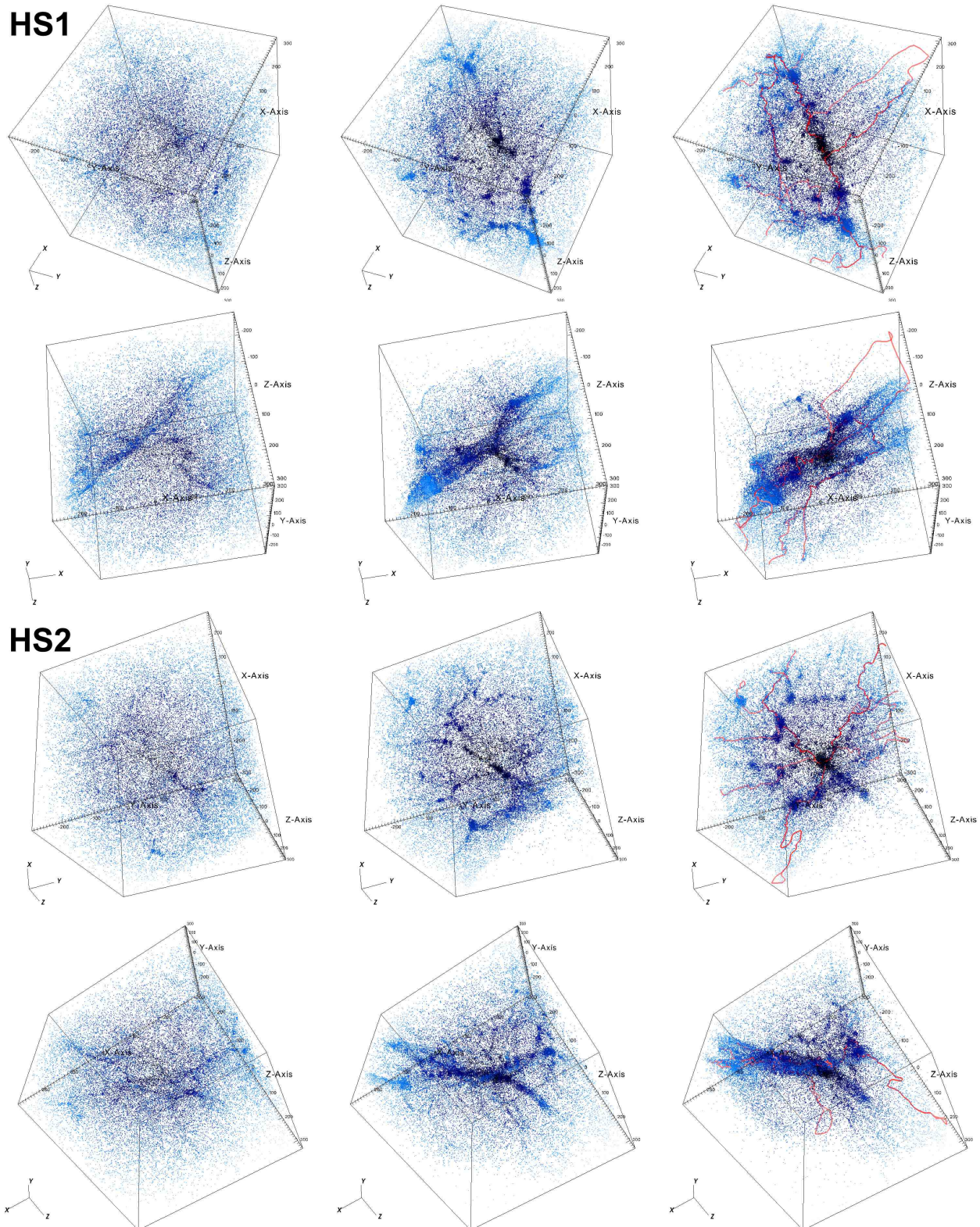
Figure 14. Same as Fig. 13 but for the HS systems. The first two rows correspond to the HS1 system and the last two rows correspond to the HS2 system. In this case the different views where selected to have a face-on view (first row) and edge-on view (second row) of the collapsed DM wall. It is clear that the environmental/filamentary structure around the central haloes is different compared to the LS system. The HS systems are located inside a filament belonging to a collapsed wall.

Fig. 13 shows the evolution for the LS systems. LS1 corresponds to the first two rows and LS2 to the last two rows. It is clear that the LS systems are located in a knot inside the cosmic web, i.e. they are located at an over-dense region surrounded by a number of converging filaments ($N_f \sim 8$). Looking at the last column of the figure, it is worth to note that the filamentary inside-out extension does not vary too much from different view angles. Such conditions constrain the accreted material to converge on the knot from different directions providing an efficient SAM cancellation inside the virial radius.

Fig. 14 shows the HS systems. HS1 corresponds to the first two rows and HS2 to the last two rows. In this case the two perpendicular views where selected to show a face-on view of the plane hosting the central halo (corresponding to the first row for each system) and an edge-on view of the same plane (corresponding to the second row for each systems). From the figure, it is possible to see how the collapse process of the wall hosting the central halo proceeds: it starts as a few parallel filaments to finish as a thick filament (an angle view effect) crossing the box. From the face-on view of both planes it is clear that the central haloes are located in a filament belonging to the collapsed wall (marked by a red line crossing the box in the last column). For HS systems, such conditions tend to constrain the accreted material to be mostly inside a filament belonging the wall. Such configuration makes the SAM cancellation process not as efficient as in the LS knot-located systems. This picture is supported by the fact that there are not too many red lines perpendicular to the DM plane associated to the wall. This feature marks a clear difference with the LS systems where there is no a preferred plane hosting the filaments.

Fig. 15 shows the angle between the DM SAM and the first two main filaments associated to the halo. Our four systems show an angle fluctuating around $90°$ for redshift $z \gtrsim 10$. It is interesting to note that mergers are correlated with sharp fluctuations of the angle. Such fluctuations are consequences of the re-configuration of the DM spin after violent merger events. Another interesting feature associated to mergers is the dispersion of the angle around $90°$. LS2 and HS1 show the larger dispersion and at the same time these two systems show the larger number of mergers which, as mentioned before, can explain such angle deviations. The $\sim 90°$ orientation can be understood in the following way: as shown before, most of the SAM is accreted through filaments onto the halo center, under such conditions any SAM component of the halo parallel to the filamentary SAM flux will be cancelled constraining the halo's SAM to a plane perpendicular to the filamentary accretion. This spin orientation mechanism is similar to the one discussed by Codis et al. (2012) in the high mass ($\gtrsim 10^{12} M_\odot$) range.

Fig 16 shows λ against the number of filaments N_f around $z = 10$ for the 4 halos simulated in this paper (diamond symbols). We found an anti-correlation between the number of filaments that converge at the DM halo and its spin value.

Despite of the small data sample (4 haloes), we can see a clear anti-correlation supporting our previous discussion. Because the above anti-correlation is so interesting, we investigated it in DM-only simulations; these consist of simulations with $N_p = 512^3$, with a particle mass of 10^6 $M_\odot$. The blue points of Fig. 16 show the dependence be-
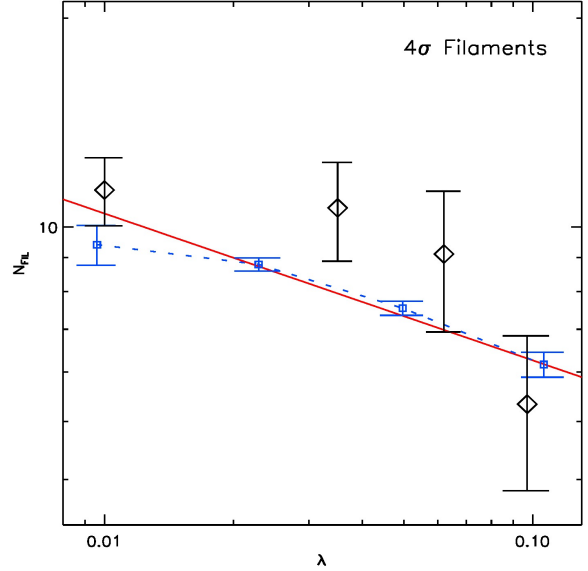

Figure 16. Average spin parameter λ as a function of the number of filaments N_f converging to the DM halo around redshift $z = 10$. Diamonds correspond to the four halos simulated in this paper including gas. The blue points are for 436 DM-only halos. There is a significant anti correlation between spin and number of filaments covering to the halo. The red solid line is the fit from eq. 10.

tween the halo spin and the number of filaments connected to the halo center. We show results for 436 halos in the mass range $5 \times 10^8 - 5 \times 10^9 M_\odot$, selecting 4 spin bins with error bars showing the 1σ uncertainty from bootstrapping. Filaments are computed using Disperse code with a 4σ detection threshold. There is a significant trend that confirms the one found with the 4 halos simulated in this paper: lower spin halos have more filaments connected to them while higher spin halos have less filaments connected them. The correlation can be written as

$$\lambda \approx 0.05 \times \left(\frac{7.6}{N_f}\right)^{5.1} \tag{10}$$

At this point it is interesting to come back to Fig. 3. The λ parameter changes significantly with redshift for each halo. In particular it is interesting to understand λ variations in both LS1 and HS2 systems. For these systems the spin parameter changes from ~ 0.1 to ~ 0.01 during their evolution. Such changes can be fully understood following the picture presented in the analysis above. The LS1 system starts with $\lambda \approx 0.03 - 0.04$ at $z \approx 20 - 16$. At this stage the main halo is inside a small filament. At $z \approx 16$ the system receives a merger through the filament increasing its spin parameter till $\lambda \gtrsim 0.1$. After that the system starts to accrete mass isotropically till it forms a clear convergent filamentary structure around it resulting in a low spin system at $z \sim 9$. The HS2 system starts with a high spin parameter at $z \approx 20 - 19$. After the merger at $z \approx 19$ the system does not belong to a filament and starts to accrete mass rather isotropically. This explains the reduction of the spin till ~ 0.01 at $z \approx 16$. At this stage the system has developed a clear filamentary structure and most of the accreted material starts to come from this preferential direc-
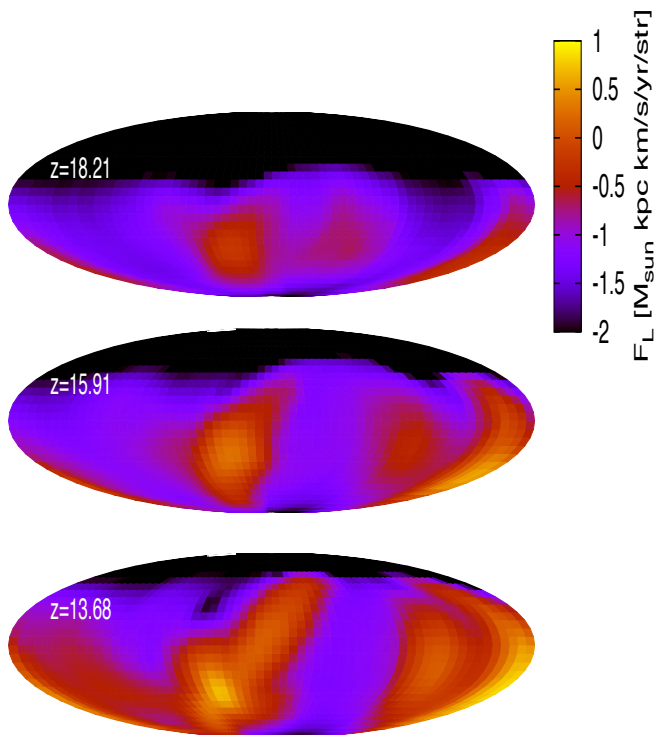
Figure 17. Mass weighted SAM flux for the HS2 system at different redshifts. The SAM accretion evolves from a rather homogeneous flux at $z = 18.21$ to a well defined filamentary accretion at $z = 13.68$ (the filament is defined by the strong accretion (yellow blob) at angle $\approx \pi/2$. This transition from an homogeneous to filamentary accretion explains the spin parameter evolution of HS2 in Fig. 3.

tion. The system continues accreting mass till the it receives two mergers at $z \gtrsim 13$ when λ reaches the value ~ 0.1; see Fig. 17.

The emerging picture from the above simulations seems to be one in which the merging process, which in turn is determined by environmental location, determines the final value of the halo spin.

4   CONCLUSIONS

We have performed numerical simulations of atomic cooling halos with the aim of understanding the origin of angular momentum in galaxies. Atomic cooling halos maybe rare objects in the sky, but they are pristine sites of galaxies formation where the complications of star formation and subsequent feedback are avoided. They therefore provide an excellent testbed to explore our theories for galaxy formation.

The numerical experiments we have performed are for four values of the halo spin parameter $\lambda = 0.01, 0.04, 0.06, 0.1$ thus sampling the 1 and 2σ ranges of the theoretically predicted LCDM probability distribution function for dark matter halos. We have shown that before turn-around the spin value of the halos follows that pre-dicted by tidal torque theory and that after turn-around the spin value is influenced by the number and direction of mergers and accreting dark matter. While this might lead one to think that after turn around the angular momentum of the gas and dark matter will be totally random, we show this not to be the case.

The final angular momentum of dark matter is strongly correlated to the morphology of the cosmic web where the halos reside. In this respect, halos with low angular momentum are those residing at the center of two or more filament crossings, while halos with high angular momentum are those residing in the middle of a filament and away from the knots of the cosmic web. There is a clear anti-correlation between the number of filaments and the final angular momentum. The physical picture that we find is that where many filaments cross, the flow of dark matter is from many directions and thus, by randomization, one ends up destroying angular momentum as it comes from different directions. On the other hand, if the halo is positioned in the middle of a filament, there is only one preferred direction from where dark and baryonic matter is accreted thus preserving the angular momentum originally determined by tidal torque theory. On the other hand, we find that the angular momentum of the gas is dominated by gradient pressures and that this causes fluctuations and misalignment with respect to the DM angular momentum, thus making it more unpredictable.

Our findings point to a picture in which the angular momentum of DM halos is obtained by features in the LCDM that are very deterministic: the rate at which other halos and dark matter are being accreted, and the morphology of the cosmic web. However, the angular momentum of the gas is driven by the gas physics itself, making it disconnected to the one of the underlying DM.

REFERENCES

Avila-Reese V., Firmani C., Hernandez X., 1998, ApJ, 505, 37

Barnes, J., & Efstathiou, G. 1987, ApJ, 319, 575

Bullock J. S., Kolatt T. S., Kravtsov A. V., Klypin A. A., Porciani C. & Primack J. R., 2001a, ApJ, 555, 240

Bromm V. & Yoshida N. 2011, ARA&A, 49, 373

P. Catelan, M. Kamionkowski, and R. D. Blandford, 2001, MNRAS 320, L7.

Catelan, P., & Porciani, C. 2001, MNRAS, 323, 713

Codis S., Pichon C., Devriendt J., Slyz A., Pogosyan D., Dubois Y. & Sousbie T., 2012, MNRAS, 427, 3320

Colberg J. M., Krughoff K. S. & Connolly A. J., 2005, MNRAS, 359, 272

Crittenden, R. G., Natarajan, P., Pen, U.-L., & Theuns, T. 2001, ApJ, 559, 552

Davis A. J., Natarajan P., 2010, MNRAS, 407, 691

Dalcanton, J. J., Spergel, D. N., & Summers, F. J. 1997, ApJ, 482, 659

Doroshkevich A. G., 1970, Afz, 6, 581

Dubois Y., Pichon C., Haehnelt M., Kimm T., Slyz A., Devriendt J., & Pogosyan D., 2012, MNRAS, 423, 3616

Fall, S. M., & Efstathiou, G. 1980, MNRAS, 193, 189

Ferrara A., 2010, AIPC, 1294, 148

Fialkov A., Barkana R., Visbal E., Tseliakhovich D., Hirata C. M., 2013, MNRAS, 432, 2909

González R. E. & Padilla N. D., 2010, MNRAS, 407, 1449

Grassi T., Bovino S., Schleicher D. R. G., Prieto J., Seifried D., Simoncini E. & Gianturco F. A., 2014, MNRAS, 439, 2386

Hahn, O., Porciani, C., Carollo, C. M., & Dekel, A. 2007, MNRAS, 375, 489

Heavens, A., & Peacock, J. 1988, MNRAS, 232, 339

Hetznecker H., Burkert A., 2006, MNRAS, 370, 1905

Jimenez, R., Heavens, A. F., Hawkins, M. R. S., & Padoan, P. 1997, MNRAS, 292, L5

Jimenez R., et al., 2010, MNRAS, 404, 975

Mo H. J., Mao S., White S. D. M., 1998, MNRAS, 295, 319

Peebles P. J. E., 1969, ApJ, 155, 393

Pichon C. & Bernardeu F., 1999, A&A, 343, 663

Pichon C., Pogosyan D., Kimm, T., Slyz, A., Devriendt, J. & Dubois, Y., 2011, MNRAS, 418, 2493

Pen, Ue-Li; Lee, Jounghun; Seljak, Uros, 2000, ApJ, 543, 107

Planck Collaboration, 2013, arXiv:1303.5076P

Porciani C., Dekel A., Hoffman Y., 2002, MNRAS, 332, 325

Prieto J. P., Infante L., Jimenez R., 2008, arXiv, arXiv:0809.2786

Prieto J., Jimenez R., Haiman Z., 2013, MNRAS, 436, 2301

Prunet S., Pichon C., Aubert D., Pogosyan D., Teyssier R. & Gottloeber S., 2008, ApJs, 178, 179

Schaefer, B. M., 2008, arXiv:0808.0203

Sousbie T., 2011, MNRAS, 414, 350

Teyssier R., 2002, A&A, 385, 337

Toomre, A. 1964, ApJ, 139, 1217

Truelove J. K., Klein R. I., McKee Ch. F., Holliman J. H., Howell L. H. & Greenough J. A., 1997, ApJl, 489, 179

Vitvitska M., Klypin A. A., Kravtsov A. V. & Wechsler R. H., 2002, ApJ, 581, 799

White, S. D. M., & Rees, M. J. 1978, MNRAS, 183, 341

White S., 1984, ApJ, 286, 38

Powell L. C., Slyz A. & Devriendt J., 2011, MNRAS, 414, 3671

APPENDIX

The Tables in this section list merger related parameters for the four halos studied in this paper. Label 1 denotes quantities associated to the main halo, while label 2 the quantities associated to the secondary progenitor, the label orb denotes quantities associated to the orbital angular momentum associated to the secondary progenitor and the label acc quantities associated to the accreted angular momentum.

Table 1. DM Merger Events.

Sim. Name	Event	z	M_1 [$M_\odot$]	$\frac{M_2}{M_1}$	J_1 [kpc km/s]	$\frac{J_2}{J_1}$	$\theta_{\vec{J}_1,\vec{J}_2}$	$\theta_{\vec{J}_1,\vec{J}_{\mathrm{orb}}}$	$\theta_{\vec{J}_1,\vec{J}_{\mathrm{acc}}}$
LS1									
	Merg1	12.68	3.89(8)	0.34	3.26(4)	0.40	137.3	104.6	64.0
	Merg2	12.86	3.46(8)	0.20	4.04(4)	0.01	55.5	134.9	24.1
	Merg3	16.17	1.03(8)	0.12	3.38(3)	0.11	67.5	51.5	36.9
	Merg4	26.75	2.98(6)	0.42	7.65(0)	0.19	112.7	157.8	139.0
Avg.				0.27		0.18	93.3	112.2	66.0
LS2									
	Merg1	9.80	1.48(9)	0.72	3.93(5)	0.15	71.9	123.6	87.9
	Merg2	11.48	7.77(8)	0.17	7.43(4)	0.15	147.6	112.3	26.6
	Merg3	14.85	1.68(8)	0.12	1.29(4)	0.03	33.0	73.4	15.5
	Merg4	15.11	1.24(8)	0.31	8.57(3)	0.04	73.5	55.6	50.0
	Merg5	15.60	9.64(7)	0.14	4.46(3)	0.02	21.4	61.3	76.8
	Merg6	16.19	7.09(7)	0.31	3.63(3)	0.16	119.5	122.2	22.9
	Merg7	16.52	6.18(7)	0.17	3.26(3)	0.07	50.9	95.2	9.7
	Merg8	17.16	4.30(7)	0.20	7.65(2)	0.08	93.2	75.3	61.5
	Merg9	21.13	3.74(6)	0.67	1.14(1)	2.57	114.1	126.9	45.9
Avg.				0.31		0.36	80.5	94.0	44.1
HS2									
	Merg1	10.16	9.73(8)	0.12	2.97(5)	0.02	26.7	64.2	4.7
	Merg2	13.06	1.82(8)	0.89	1.42(4)	0.83	126.1	36.6	20.8
	Merg3	13.67	1.42(8)	0.38	7.99(3)	0.12	115.1	19.7	5.6
	Merg4	19.36	4.08(6)	1.07	1.98(1)	1.85	74.9	86.3	76.0
Avg.				0.62		0.71	85.7	51.7	26.8
HS1									
	Merg1	10.04	8.21(8)	0.48	1.84(5)	0.20	105.1	27.2	18.7
	Merg2	11.34	4.31(8)	0.29	3.61(4)	0.26	154.4	152.0	52.9
	Merg3	13.26	9.13(7)	0.64	5.93(3)	0.67	23.6	116.6	119.4
	Merg4	15.33	3.10(7)	0.49	5.93(2)	0.78	132.8	129.2	143.6
	Merg5	15.65	2.72(7)	0.22	7.07(2)	0.80	101.2	175.8	14.9
	Merg6	18.13	7.57(6)	0.61	8.48(1)	0.38	129.3	114.3	130.8
	Merg7	18.56	5.78(6)	0.26	5.54(1)	0.11	129.4	134.9	13.9
	Merg8	20.22	2.26(6)	0.52	1.02(1)	0.23	123.1	104.4	59.1
Avg.				0.44		0.43	112.4	119.3	69.2

Table 2. Gas Merger Events.

Sim. Name	Event	z	M_1 [$M_\odot$]	$\frac{M_2}{M_1}$	J_1 [kpc km/s]	$\frac{J_2}{J_1}$	$\theta_{\vec{J}_1,\vec{J}_2}$	$\theta_{\vec{J}_1,\vec{J}_{orb}}$	$\theta_{\vec{J}_1,\vec{J}_{acc}}$
LS1									
	Merg1	12.68	6.31(7)	0.36	2.41(4)	0.54	135.5	100.9	68.1
	Merg2	12.86	5.62(7)	0.26	2.46(4)	0.07	28.9	143.8	5.5
	Merg3	16.17	1.64(7)	0.11	2.56(3)	0.10	43.7	61.8	38.3
	Merg4	26.75	2.82(5)	0.24	1.35(0)	0.42	78.5	125.2	96.9
Avg.				0.24		0.28	71.7	107.9	52.2
LS2									
	Merg1	9.80	2.56(8)	0.73	5.47(5)	0.39	5.3	48.4	3.9
	Merg2	11.48	1.28(8)	0.22	7.37(4)	0.28	156.1	139.1	9.7
	Merg3	14.85	2.54(7)	0.12	1.13(4)	0.04	54.2	76.6	23.2
	Merg4	15.11	2.19(7)	0.30	1.31(4)	0.02	98.4	73.0	25.4
	Merg5	15.60	1.58(7)	0.13	5.42(3)	0.02	23.6	25.1	44.6
	Merg6	16.19	1.13(7)	0.29	4.27(3)	0.07	106.4	143.3	9.1
	Merg7	16.52	9.46(6)	0.21	2.66(3)	0.07	131.6	136.5	11.3
	Merg8	17.16	6.57(6)	0.16	8.94(2)	0.02	59.6	74.1	54.2
	Merg9	21.13	4.92(5)	0.59	1.79(0)	0.83	82.4	64.8	73.4
Avg.				0.31		0.19	79.7	86.8	28.3
HS2									
	Merg1	10.16	1.65(8)	0.11	2.51(5)	0.05	25.8	56.6	4.1
	Merg2	13.06	2.85(7)	0.95	9.13(3)	1.35	115.0	71.9	60.1
	Merg3	13.67	2.22(7)	0.43	5.54(3)	0.32	90.1	44.0	12.7
	Merg4	19.36	5.60(5)	0.73	1.10(1)	0.82	92.5	86.5	64.4
Avg.				0.56		0.64	80.9	64.8	35.3
HS1									
	Merg1	10.04	1.41(8)	0.57	2.41(5)	0.17	91.2	31.3	9.2
	Merg2	11.34	7.02(7)	0.31	4.18(4)	0.30	166.2	155.9	18.9
	Merg3	13.26	1.54(7)	0.63	3.79(3)	1.09	43.3	108.7	110.9
	Merg4	15.33	4.52(6)	0.48	6.66(2)	0.38	89.0	115.2	129.7
	Merg5	15.65	3.92(6)	0.22	6.78(2)	0.07	112.4	165.5	15.2
	Merg6	18.13	1.01(6)	0.54	3.03(1)	0.48	45.1	55.1	67.4
	Merg7	18.56	6.86(5)	0.21	1.74(1)	0.07	20.1	85.3	5.7
	Merg8	20.22	2.04(5)	0.41	2.49(0)	0.35	146.6	66.6	51.2
Avg.				0.42		0.36	89.2	98.0	51.0